Strong Depletion of 13C in CO Induced by Photolysis of CO2 in the Martian Atmosphere, Calculated by a Photochemical Model

Tatsuya Yoshida, Shohei Aoki, Yuichiro Ueno, Naoki Terada, Yuki Nakamura, Kimie Shiobara, Nao Yoshida, Hiromu Nakagawa, Shotaro Sakai, Shungo Koyama

The Planetary Science Journal, 4:53 (8pp), 2023 March https://doi.org/10.3847/PSJ/acc030

Strong Depletion of ^{13}C in CO Induced by Photolysis of CO_2 in the Martian Atmosphere, Calculated by a Photochemical Model

Tatsuya Yoshida[1], Shohei Aoki[2], Yuichiro Ueno[3,4,5], Naoki Terada[1], Yuki Nakamura[1,6], Kimie Shiobara[1], Nao Yoshida[1], Hiromu Nakagawa[1], Shotaro Sakai[1], and Shungo Koyama[1]
[1] Department of Geophysics, Graduate School of Science, Tohoku University, Sendai, Miyagi 980-8578, Japan
[2] Department of Complexity Science and Engineering, Graduate School of Frontier Sciences, University of Tokyo, Kashiwa, Chiba 277-8561, Japan
[3] Department of Earth and Planetary Sciences, Tokyo Institute of Technology, Meguro, Tokyo 152-8551, Japan
[4] Earth-Life Science Institute (WPI-ELSI), Tokyo Institute of Technology, Meguro, Tokyo 152-8550, Japan
[5] Japan Agency for Marine-Earth Science and Technology (JAMSTEC), Yokosuka, Kanagawa 237-0061, Japan
[6] LATMOS, Sorbonne Université, 75005 Paris, France
Received 2022 September 22; revised 2023 February 21; accepted 2023 February 23; published 2023 March 22

Abstract

The isotopic signature of atmospheric carbon offers a unique tracer for the history of the Martian atmosphere and the origin of organic matter on Mars. The photolysis of CO_2 is known to induce strong isotopic fractionation of the carbon between CO_2 and CO. However, its effects on the carbon isotopic compositions in the Martian atmosphere remain uncertain. Here, we develop a 1D photochemical model to consider the isotopic fractionation via photolysis of CO_2, to estimate the vertical profiles of the carbon isotopic compositions of CO and CO_2 in the Martian atmosphere. We find that CO is depleted in ^{13}C compared with CO_2 at each altitude, due to the fractionation via CO_2 photolysis: the minimum value of the $\delta^{13}C$ in CO is about −170‰ under the standard eddy diffusion setting. This result supports the hypothesis that fractionated atmospheric CO is responsible for the production of the ^{13}C-depleted organic carbon in the Martian sediments detected by the Curiosity Rover, through the conversion of CO into organic materials and their deposition on the surface. The photolysis and transport-induced fractionation of CO that we report here leads to a ∼15% decrease in the amount of inferred atmospheric loss when combined with the present-day fractionation of the atmosphere and previous studies of carbon escape to space. The fractionated isotopic composition of CO in the Martian atmosphere may be observed by ExoMars Trace Gas Orbiter and ground-based telescopes, and the escaping ion species produced by the fractionated carbon-bearing species may be detected by the Martian Moons eXploration mission in the future.

Unified Astronomy Thesaurus concepts: Planetary atmospheres (1244)

1. Introduction

Isotopic compositions of volatiles have been used to trace histories of planetary atmospheres. The enrichment in the heavy isotopes of the atmospheric components, such as hydrogen, carbon, nitrogen, and the noble gases of Mars, with respect to Earth and primitive meteorites, indicates that Mars has lost a large portion of its atmosphere via atmospheric escape processes (e.g., Owen et al. 1977; Jakosky 1991; Pepin 1991, 1994; Jakosky et al. 1994; Hu et al. 2015; Kurokawa et al. 2018).

The isotopic signatures of carbon-bearing species offer unique tracers for the atmospheric evolution of Mars, since CO_2 is the major constituent of the Martian atmosphere (Hu et al. 2015). Hu et al. (2015) have modeled the isotopic fractionation of the carbon induced by atmospheric escape processes—such as photochemical escape and solar wind–induced sputtering, depositions of carbonate minerals, and volcanic outgassing—to trace the evolution of the carbon reservoir and its isotopic composition, to satisfy the present-day carbon isotopic ratio of CO_2 in the atmosphere, as observed by the Curiosity Rover. In their calculation, atmospheric escape, especially photochemical escape via CO photodissociation, enriches the heavy carbon (^{13}C) in the atmosphere efficiently, which can drive the carbon isotopic ratio to the present-day fractionated value.

In addition to the isotopic fractionation processes considered by Hu et al. (2015), photolysis of CO_2 is expected to affect the isotopic compositions of carbon-bearing species significantly. Schmidt et al. (2013) have demonstrated that the UV absorption cross section of $^{13}CO_2$ is lower than that of $^{12}CO_2$ by several hundred per mil in the wavelength range of 138–212 nm, using a quantum mechanical methodology. This suggests that photolysis of CO_2 could induce isotopic fractionation between CO_2 and carbon-bearing photochemical products, such as CO, in the troposphere and stratosphere by several hundred per mil. The degree of fractionation is much higher than those of the other known isotopic fractionation processes. For example, the condensation of carbonate minerals, one of the other fractionation processes of carbon, enriches the carbon isotopic ratio of carbonate precipitates by only ∼10‰ relative to the source atmosphere (Hu et al. 2015). However, the effects of photoinduced isotopic fractionation on the carbon isotopic composition in the Martian atmosphere have not been investigated quantitatively.

The photoinduced carbon isotopic fractionation in CO may be related to the carbon isotopic composition of organic carbon in Martian sediments. It has been predicted that ^{13}C-depleted organic materials could have been deposited on the surface, if their photochemical production via CO as an intermediate proceeded efficiently on early Mars (Lammer et al. 2020; Stueeken et al. 2020). As expected, the Curiosity Rover found

that sedimentary organic carbon at Gale crater with an age of ∼3.5 billion yr was depleted in ^{13}C by more than ∼100‰ compared with the atmosphere (House et al. 2022). In response to this, Ueno et al. (2022) have suggested that the atmospheric synthesis of organic materials from CO is a plausible mechanism for explaining the presence of organic carbon in early Martian sediments and its strong ^{13}C depletion, through experimental and theoretical studies of the photolysis of CO_2. To validate this hypothesis, quantitative estimates of the carbon isotopic composition in CO, considering chemical kinetics and transport in the atmosphere, are needed.

The photoinduced carbon isotopic fractionation in CO may also affect the degree of isotopic fractionation by atmospheric escape. The photodissociation of CO is the most important photochemical source of escaping carbon atoms from Mars (Fox & Bakalian 2001; Groller et al. 2014; Lo et al. 2021). Here, the vertical transport of the fractionated CO to the upper atmosphere near the escape region should lead to a change in the fractionation factor of the photochemical escape via CO photodissociation.

In this study, we develop a 1D atmospheric photochemical model that considers the isotopic fractionation from the photolysis of CO_2 in order to quantitatively estimate the vertical profiles of the carbon isotopic compositions of CO and CO_2. This allows us to clarify the effects of the photolysis on the isotopic compositions. This paper is organized as follows. In Section 2, we describe the outline of our 1D photochemical model. In Section 3, we show the numerical results of the atmospheric profiles. In Section 4.1, we discuss the dependencies of the isotopic composition profiles on the magnitudes of the eddy diffusion coefficients. In Section 4.2, we discuss the relationship between the fractionated atmospheric CO and the ^{13}C-depleted organic carbon in Martian sediments. In Section 4.3, we discuss the effects of the fractionation via photolysis on the degree of fractionation via atmospheric escape. In Section 4.4, the detectability of the calculated isotopic fractionation in CO using existing measurements is discussed.

2. Model Description

We use a 1D photochemical model developed by Nakamura et al. (2022a, 2022b), with some modifications to the chemical processes. These solve the continuity-transport equations that govern the changes in the number density profiles of the chemical species, by numerical integration over time, until the profiles settle into steady states. As for the chemical processes, 57 chemical reactions are considered for 17 species: $^{12}CO_2$, $^{13}CO_2$, ^{12}CO, ^{13}CO, H_2O, O, O(^{1}D), H, OH, H_2, O_3, O_2, HO_2, H_2O_2, $HO^{12}CO$, $HO^{13}CO$, and $^{12}CO_2^+$ (Table A1). Here, we refer to the chemical species and reactions considered by Chaffin et al. (2017). We newly include minor carbon-bearing isotopologues, such as $^{13}CO_2$, ^{13}CO, and $HO^{13}CO$, and their chemical reactions. To calculate the profiles of the photolysis rates, we adopt the solar spectrum profile in the wavelength range from 0.5 to 1100 nm, as obtained by Woods et al. (2009), and solve the radiative transfer by considering the absorption of the solar irradiation by chemical species. We adopt the absorption cross section of $^{12}CO_2$ and $^{13}CO_2$ at 138–212 nm, as provided by Schmidt et al. (2013), to estimate the isotopic fractionation through photolysis. For the absorption cross sections of $^{12}CO_2$ and $^{13}CO_2$ in other wavelengths, we refer to Huestis & Berkowitz (2011), and the references therein. For the absorption cross sections of the other chemical species, we mainly refer to the JPL publication (Burkholder et al. 2015) and the MPI-Mainz UV/VIS Spectral Atlas of Gaseous Molecules (Keller-Rudek et al. 2013).[7] The spectral bin at 138–212 nm is 0.1 nm, to resolve the difference in the photolysis rate between $^{12}CO_2$ and $^{13}CO_2$, and that at the other wavelengths is 1 nm. We also consider the difference in rate coefficients of the chemical reactions between ^{12}CO and ^{13}CO: the rate coefficient of the reaction of ^{13}CO with O (R22 in Table A1) is 1.007 times as large as that for ^{12}CO (R21; Ueno et al. 2022), and the rate coefficients of the reactions of ^{13}CO with OH (R52 and R54) are 0.989 times as large as those for ^{12}CO (R51 and R53; Feilberg et al. 2005). In addition, the rate coefficient of the reaction of $HO^{13}CO$ with O_2 (R56) is assumed to be 0.989 times as large as that of $HO^{12}CO$ (R55), by referring to the differences in the rate coefficients between R51(R53) and R52 (R54). We adopt the fixed number density profile of H_2O used by Koyama et al. (2021). Here, the relative humidity below 30 km is fixed at 22%, to give 9.5 precipitable microns of water, and the H_2O profile above is connected to the saturation water vapor at the altitude where the temperature is at the minimum; the same mixing ratio is then assumed above higher altitudes. The number density profile of $^{12}CO_2^+$ is fixed as the standard case from Chaffin et al. (2017). The profiles for the temperature, eddy diffusion coefficient, and binary diffusion coefficient are taken from Chaffin et al. (2017).

The lower boundary is set at the planetary surface. The number densities of $^{12}CO_2$ and $^{13}CO_2$ at the lower boundary are fixed at $2.10 \times 10^{17}\,cm^{-3}$ (Chaffin et al. 2017) and $2.46 \times 10^{15}\,cm^{-3}$, respectively, to satisfy the carbon isotopic ratio in CO_2 measured by the Sample Analysis at Mars Tunable Laser Spectrometer (SAM/TLS) on the Curiosity Rover (Webster et al. 2013). The altitude of the upper boundary is set at 200 km. As the upper boundary condition, H and H_2 are assumed to escape to space by Jeans escape, and the O escape rate is fixed at $1.2 \times 10^8\,cm^{-2}\,s^{-1}$, as in Chaffin et al. (2017).

3. Results

The number density profiles of each chemical species in the steady state are shown in Figure 1. The calculated profiles of the major isotopologues are in good agreement with Chaffin et al. (2017), except for the slight differences in the abundances of odd hydrogen and odd oxygen, caused by the differences in the adopted absorption cross sections and H_2O profile. Figure 2 represents the profiles of the carbon isotopic ratios in CO and CO_2. Here, the carbon isotopic ratios are expressed by the deviation of the calculated ratio with respect to the standard ratio, in units per mil:

$$\delta^{13}C = \left(\frac{R}{R_s} - 1\right) \times 1000, \quad (1)$$

where R is the $^{13}C/^{12}C$ ratio and $R_s = 1.123 \times 10^{-2}$, which is the $^{13}C/^{12}C$ ratio of the Vienna Pee Dee Belemnite. As shown in Figure 2, CO has lower $\delta^{13}C$ than CO_2 at each altitude, because the photolysis of CO_2, which is the main formation reaction of CO, involves the isotopic fractionation of carbon between CO_2 and CO, due to the difference in the absorption cross section between $^{12}CO_2$ and $^{13}CO_2$ (Schmidt et al. 2013; Figure 3).

[7] https://www.uv-vis-spectral-atlas-mainz.org/uvvis/

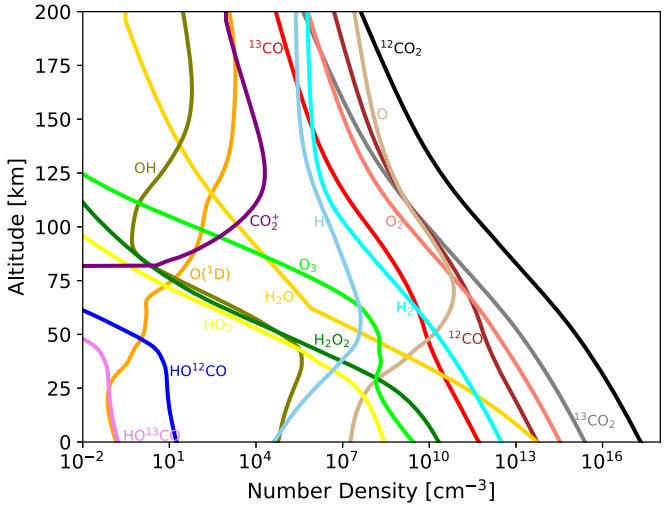

Figure 1. Number density profiles of each chemical species.

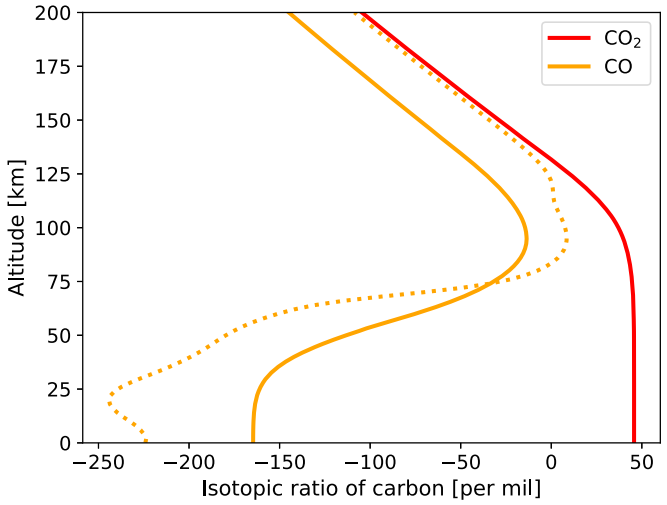

Figure 2. Profiles of the carbon isotopic ratios in CO and CO_2. The isotopic ratios are expressed by the deviation of the calculated ratio with respect to the standard ratio, in units per mil: $\delta^{13}C = \left(\frac{R}{R_s} - 1\right) \times 1000$, where R is the $^{13}C/^{12}C$ ratio and $R_s = 1.123 \times 10^{-2}$. The solid orange line and the solid red line represent the carbon isotopic ratios in CO and CO_2, respectively. The dotted orange line represents the ratio of the photolysis rate of $^{13}CO_2$ to that of $^{12}CO_2$, which approximates the isotopic ratio of CO, when assuming the local photochemical equilibrium without vertical transport.

Below ∼100 km, the $\delta^{13}C$ in CO decreases as the altitude decreases: it takes the minimum value of about −170‰ near the surface. The degree of isotopic fractionation is much higher than those of other fractionation processes, such as the condensation of carbonate minerals (Hu et al. 2015). The reason why the $\delta^{13}C$ in CO decreases with decreasing altitude is because the wavelength of the absorbed solar irradiation is longer in the lower region (Figure 3(a)), where the difference in the absorption cross sections between $^{12}CO_2$ and $^{13}CO_2$ is large (Figures 3(b) and (c)).

The carbon isotopic ratio in CO_2 below ∼100 km is constant at the surface value of 46‰, which is assumed to be equal to the value measured by SAM/TLS on the Curiosity Rover. On the other hand, the average $\delta^{13}C$ in the altitude range of 70–90 km as measured by the Atmospheric Chemistry Suite (ACS) on board the ExoMars Trace Gas Orbiter (TGO) is -3 ± 37‰ (Alday

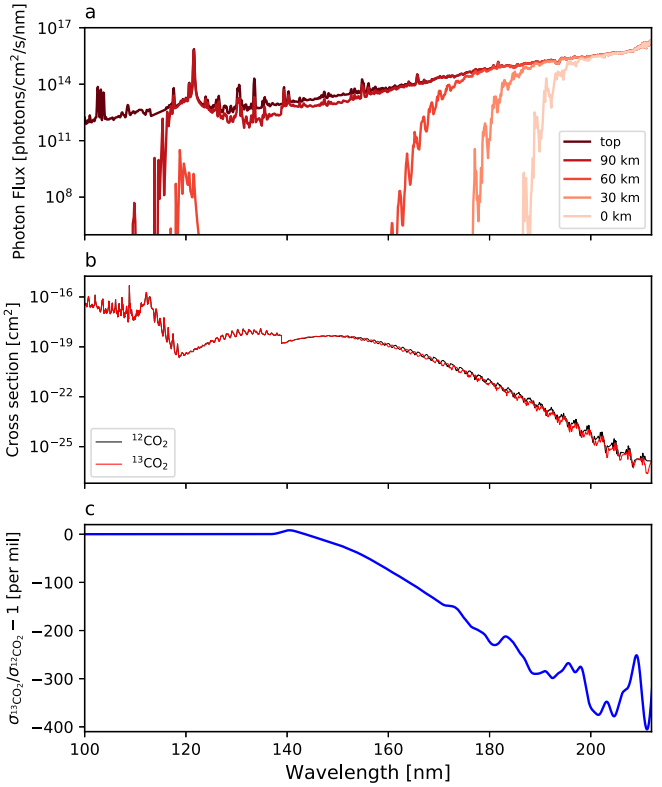

Figure 3. (a) Profiles of the photon flux with wavelength at each altitude. (b) Absorption cross sections of $^{12}CO_2$ and $^{13}CO_2$ with wavelength. The black and red lines represent the absorption cross sections of $^{12}CO_2$ and $^{13}CO_2$, respectively. (c) The relative difference of the absorption cross sections between $^{12}CO_2$ and $^{13}CO_2$: $(\sigma_{^{13}CO_2}/\sigma_{^{12}CO_2} - 1) \times 1000$, where $\sigma_{^{12}CO_2}$ and $\sigma_{^{13}CO_2}$ are the absorption cross sections of $^{12}CO_2$ and $^{13}CO_2$, respectively. Here, the relative difference is averaged over a Gaussian window with FWHMs of 2.5 nm, as done by Schmidt et al. (2013).

et al. 2021). The reason for the difference in the evaluated carbon isotopic ratio in CO_2 between our model (SAM/TLS) and ACS remains uncertain. Alday et al. (2021) have suggested two scenarios for reconciling the measurements from SAM/TLS and ACS, as follows. One possible scenario requires the presence of unknown isotopic fractionation processes between the lower and upper atmospheres of Mars: ACS measures the carbon isotopic ratio above 70 km, while the Curiosity Rover measures that on the surface. The other relies on the impact of climatological isotopic fractionation: the ACS measurements extend over a large range of locations, seasons, and local times, allowing averaging over hundreds of measurements, from which the effects of climatological fractionation are expected to be small, while the measurements made by the Curiosity Rover are always made in the same location, at roughly the same local time.

The $\delta^{13}C$ in both CO and CO_2 decreases as the altitude increases above ∼100 km, which corresponds to the altitude of the homopause, due to the diffusive separation that results from the differences in molecular mass between isotopologues. The calculated isotopic fractionation of CO_2 in the upper region above ∼100 km is consistent with the profile observed by ACS (Alday et al. 2021).

The dotted line in Figure 2 represents the ratio of the photolysis rate of $^{13}CO_2$ to that of $^{12}CO_2$, which approximates the isotopic ratio of CO, when assuming the local photochemical equilibrium without vertical transport. The difference between the dotted orange line and the solid orange line shows the effect

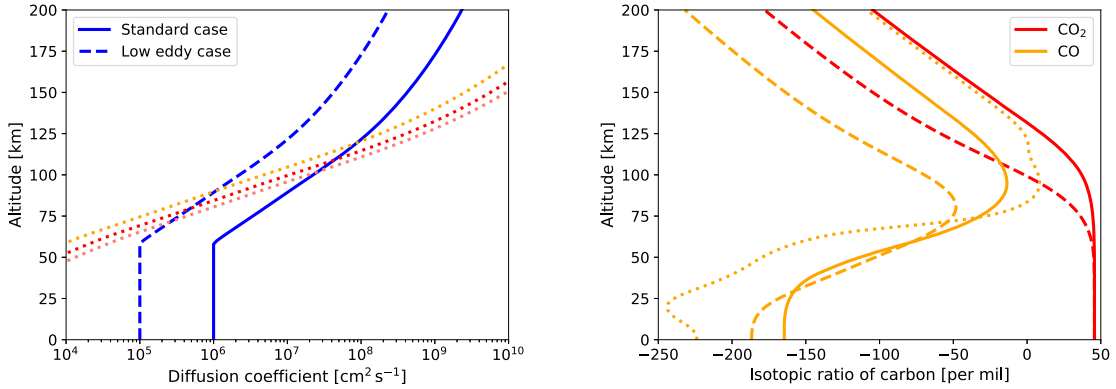

Figure 4. (a) Profiles of the eddy diffusion coefficient and the molecular diffusion coefficient. The solid blue line represents the profile of the eddy diffusion coefficient under the standard setting (the "Standard case"), while the dashed blue line represents that 10 times as small as the standard setting (the "Low eddy case"). The dotted orange, red, and pink lines represent the profiles of the molecular diffusion coefficients of O, H_2, and H, respectively. (b) Profiles of the carbon isotopic ratios in CO and CO_2, depending on the magnitude of the eddy diffusion coefficient. The isotopic ratios are expressed by the deviation of the calculated ratio with respect to the standard ratio in units per mil: $\delta^{13}C = \left(\frac{R}{R_s} - 1\right) \times 1000$, where R is the $^{13}C/^{12}C$ ratio and $R_s = 1.123 \times 10^{-2}$. The solid lines and dashed lines show the results under the standard eddy diffusion setting and those under the eddy diffusion coefficient 10 times as small as the standard setting, respectively. The orange lines and red lines represent the carbon isotopic ratios in CO and CO_2, respectively. The dotted orange line is the same as that in Figure 2, which represents the isotopic ratio of CO on the assumption of the local photochemical equilibrium.

of the vertical transport due to diffusion on the profile of the CO isotopic composition: the vertical transport dilutes the difference in the isotopic composition among altitudes.

4. Discussion

4.1. Effects of Changes in the Magnitude of the Eddy Diffusion Coefficient on the Atmospheric Profile

The eddy diffusion coefficient in the Martian atmosphere is estimated to be variable with season and latitude (Yoshida et al. 2022). The change in the eddy diffusion coefficient affects the atmospheric profile, including the isotopic composition. Figure 4 compares the profiles of the carbon isotopic ratios of CO and CO_2 under an eddy diffusion coefficient that is 10 times as small as the standard setting with those under the standard setting. Below ~25 km, the $\delta^{13}C$ in CO becomes lower under the lower eddy diffusion coefficient, due to the suppression of the dilution of the difference in isotopic composition among altitudes by vertical transport. In the upper region above ~75 km, the $\delta^{13}C$ in both CO and CO_2 becomes lower, due to the more efficient diffusive separation through molecular diffusion relative to the mixing by eddy diffusion. To the contrary, under a higher eddy diffusion coefficient, the dilution of the difference in the isotopic composition among altitudes is enhanced, and the diffusive separation through molecular diffusion is suppressed.

4.2. Relationship between the Fractionated Atmospheric CO and ^{13}C-depleted Organic Carbon in Martian Sediments

Our results of CO being depleted in ^{13}C support the hypothesis that the photochemical production and deposition of organic materials via CO is responsible for producing the ^{13}C-depleted organic carbon in Martian sediments (Lammer et al. 2020; Stueeken et al. 2020; Ueno et al. 2022). The main organic molecule produced in an early Martian CO_2-dominated atmosphere should be formaldehyde (H_2CO), which can be produced as follows (e.g., Pinto et al. 1980):

$$H + CO + M \rightarrow HCO + M, \quad (2)$$

$$HCO + HCO + M \rightarrow H_2CO + CO + M, \quad (3)$$

where M is the third body. Considering the production processes, the ^{13}C-depleted isotopic composition of CO is expected to be transferred to formaldehyde. Assuming that formaldehyde has the same isotopic composition as CO, our results can explain the existence of organic carbon with $\delta^{13}C$ lower than −100‰, as detected by the Curiosity Rover. On the other hand, this study does not suppose an early Martian atmosphere condition in which organic materials could have been produced. Our future work will estimate the deposition rates and isotopic compositions of organic molecules, such as formaldehyde, in the condition of early Mars.

4.3. Effects of the Carbon Isotopic Fractionation in CO on the Fractionation through Photochemical Escape

The carbon isotopic fractionation between the lower atmosphere and the escape region is expected to affect the degree of fractionation through atmospheric escape. In this section, we roughly estimate the effect by using the framework of Rayleigh fractionation (Rayleigh 1896; Hunten 1982). As for the atmospheric escape processes, we only consider photochemical escape via CO photodissociation, which is the dominant process for the production of escaping carbon atoms on Mars (e.g., Fox & Bakalian 2001; Groller et al. 2014; Lo et al. 2021). The relationship between the isotopic ratio and the fractionation factor is given by

$$\frac{R}{R_0} = \left(\frac{N_{^{12}C}}{N^0_{^{12}C}}\right)^{f-1}, \quad (4)$$

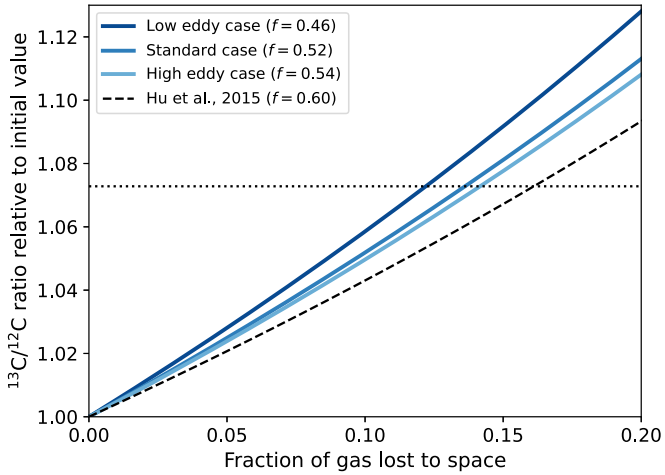

Figure 5. $^{13}C/^{12}C$ ratio relative to the initial value in the whole atmosphere as a function of the fraction of gas lost to space for each fractionation factor, for the standard eddy diffusion coefficient setting (the "Standard case"), the eddy diffusion coefficient 10 times as small as the standard setting (the "Low eddy case"), the eddy diffusion coefficient 10 times as large as the standard setting (the "High eddy case"), and the setting of Hu et al. (2015; "Hu et al., 2015"), respectively. The dotted black line represents the $^{13}C/^{12}C$ ratio of the present Martian atmosphere relative to that of the mantle-degassed CO_2 derived from the magmatic component of the SNC meteorites (Hu et al. 2015).

where R and R_0 are the $^{13}C/^{12}C$ ratio, its initial value in the whole atmosphere, f, is the fractionation factor, and $N_{^{12}C}$ and $N^0_{^{12}C}$ are the total inventory of ^{12}C and its initial value. Here, we define the net fractionation factor as follows:

$$f = f_{s-e} \times f_{esc}, \quad (5)$$

where f_{s-e} is the fractionation factor between the surface and the escape region, which is the ratio of $^{13}C/^{12}C$ in CO at the escape region to that in CO_2 at the surface, and f_{esc} is the fractionation factor by atmospheric escape. We assume that the fractionation factor by photochemical escape via CO photodissociation f_{esc} is 0.6, referring to Hu et al. (2015), and that the altitude of the escape region is 160 km, where the production of escaping atoms typically peaks (e.g., Fox & Hac 2009; Lo et al. 2021). The net fractionation factor f under the standard eddy diffusion setting is 0.52. It highly depends on the magnitude of the eddy diffusion coefficient. For example, $f = 0.46(0.54)$ under the eddy diffusion coefficient 10 times as small (large) as the standard setting.

Figure 5 shows the $^{13}C/^{12}C$ ratio relative to the initial value in the whole atmosphere as a function of the fraction of gas lost to space. The carbon fractionation when considering the isotopic fractionation between the lower atmosphere and the escape region proceeds more efficiently than the estimates by Hu et al. (2015). The $^{13}C/^{12}C$ ratio of the present Martian CO_2 atmosphere is higher by a factor of about 1.07 than that of the mantle-degassed CO_2 derived from the magmatic component of SNC meteorites (Hu et al. 2015). Beginning with an atmospheric $^{13}C/^{12}C$ ratio equal to that of the mantle-degassed CO_2, the effective carbon isotopic fractionation through photochemical escape can drive the carbon isotopic ratio to the present-day fractionated value, even when the amount lost by atmospheric escape is small compared with that evaluated by Hu et al. (2015). On the other hand, there are various isotopic fractionation processes, such as other atmospheric escape processes, like solar wind–induced sputtering and ion pickup, volcanic outgassing, depositions of carbonate minerals and organic matter, and so on. Our future work will estimate the evolution of the carbon reservoir and its isotopic composition by considering these processes comprehensively.

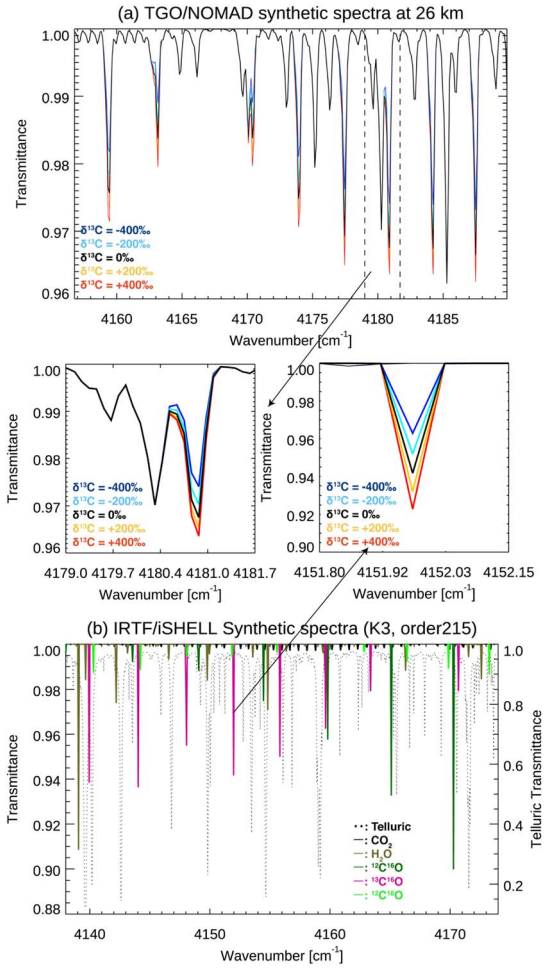

Figure 6. (a) Synthetic spectra of a solar occultation measurement by TGO/NOMAD, taken with diffraction order 186. The calculations are performed using the Asimut radiative transfer and retrieval code (Vandaele et al. 2006). The simulation is made for a measurement at 26 km over the northern polar region (latitude: 82°N) at Ls = 165°. The atmospheric condition is obtained from GEM-Mars (Daerden et al. 2019). The CO volume mixing ratio at 26 km is assumed to be 776 ppm. The differences in color represent the assumed isotopic ratios for the ^{13}CO lines (blue: $\delta^{13}C = -400‰$; light blue: $\delta^{13}C = -200‰$; black: $\delta^{13}C = 0‰$; orange: $\delta^{13}C = +200‰$; and red: $\delta^{13}C = 400‰$). The rest of the strong features are due to ^{12}CO. The upper panel shows the whole spectral range of order 186, while the small panel below is for a limited spectral range that contains both ^{12}CO and ^{13}CO lines. The typical S/N of a single NOMAD spectrum is more than 1000, which suggests that the strong depletion of ^{13}C presented by this study may be observed with TGO/NOMAD. (b) Synthetic spectra of a measurement by IRTF/iSHELL, taken with diffraction order 215 in the K3 band. The calculations are performed using the online version of PSG (Villanueva et al. 2018). In the calculation, a typical atmospheric condition at the Mars equatorial regions (the volume mixing ratio of CO is 700 ppm) is assumed. The lower panel shows the features due to CO_2 (the black curve), H_2O (the dark yellow curve), $^{12}C^{16}O$ (the dark green curve), $^{13}C^{16}O$ (the purple curve), and $^{12}C^{18}O$ (the light green curve). The expected telluric transmittance at the Maunakea observatory (where the IRTF telescope is located) is presented as the dotted dotted curve. The small panel above shows the $^{13}C^{16}O$ lines at 4 151.97 cm^{-1} for different isotopic ratios (blue: $\delta^{13}C = -400‰$; light blue: $\delta^{13}C = -200‰$; black: $\delta^{13}C = 0‰$; orange: $\delta^{13}C = +200‰$; and red: $\delta^{13}C = 400‰$). The typical S/N of a Mars spectrum taken by IRTF/iSHELL over a few pixels (which corresponds to 0.1″) is more than 100, which suggests that the strong depletion of ^{13}C presented in this study may be also observed by IRTF/iSHELL.

4.4. Possibility of Observing the Fractionated Carbon Isotopic Composition

Even though a relatively strong depletion of ^{13}C in CO is suggested by our calculations, the isotopic ratio between ^{12}CO and ^{13}CO has not been quantified by previous observations. Strong ^{12}CO and ^{13}CO lines are available in the near-IR spectral range, at 4140–4220 cm^{-1}, which can be used to measure the isotopic ratio. For that, high-resolution spectroscopy is required, since the lines of ^{12}CO and ^{13}CO in the spectral range are quite narrow under the condition of the Mars atmosphere. The spectrometers on board the ExoMars TGO, Nadir and Occultation for Mars Discovery (NOMAD; Vandaele et al. 2018), and the ACS (Korablev et al. 2018) are able to perform such spectroscopic measurements of these spectral ranges at relatively high spectral resolutions ($R \sim 16{,}000$–$50{,}000$). These instruments perform solar occultation measurements, making it possible to achieve high signal-to-noise ratios (S/Ns; >1000) and investigate the vertical profiles of trace gas. In fact, these instruments have revealed the vertical profiles of D/H and $^{18}O/^{17}O/^{16}O$ in water vapor (Alday et al. 2021; Villanueva et al. 2021, 2022) and $^{13}C/^{12}C$ and $^{18}O/^{17}O/^{16}O$ in CO_2 (Alday et al. 2021), while measuring $^{13}C/^{12}C$ in CO has been listed as one of the science targets (Vandaele et al. 2018). Figure 6(a) shows the expected NOMAD spectra at 26 km, as calculated by the Asimut radiative transfer code (Vandaele et al. 2006; Aoki et al. 2019). The S/N of the NOMAD spectrum is typically greater than 1000 for a single spectrum, thus the synthetic spectra shown in Figure 6(a) demonstrate that the strong depletion of ^{13}C in CO, as suggested by our calculations, could be identified by the NOMAD observations. The other potential platform for measuring $^{13}C/^{12}C$ in CO is by means of a high–spectral resolution spectrograph installed at a large ground-based telescope (such as IRTF/iSHELL, Very Large Telescope/CRIRES+, etc.). They cannot perform solar occultation measurements, but the spectral resolutions of these instruments are about two to five times better than those of NOMAD and ACS. Figure 6(b) shows the expected IRTF/iSHELL spectra, as calculated by the Planetary Spectrum Generator (PSG) radiative transfer code (Villanueva et al. 2018). The S/N of a Mars spectrum taken by IRTF/iSHELL, with binning over a few pixels (corresponding to $\sim 1\farcs0$), is typically greater than 100. Given that the angular diameter of Mars is greater than $10''$ in an optimal observation period, the global average of the retrievals could be used to detect the suggested depletion of ^{13}C in CO with IRTF/iSHELL. Note that the signal from Mars is attenuated by the absorption due to the telluric atmosphere (shown as the black dotted curve in Figure 6(b)), but the target CO features do not heavily overlap with the telluric features. Moreover, the telluric features can be removed by modeling them with radiative transfer calculations (see, e.g., Villanueva et al. 2013).

Our results suggest that the degree of isotopic fractionation of escaping carbon is enhanced through the vertical transport of fractionated CO to the upper atmosphere near the escape region (Section 4.3). Recently, fluxes of C^+ in the Martian magnetotail have been detected by the Mars Atmospheric and Volatile EvolutioN SupraThermal And Thermal Ion Composition (Pickett et al. 2022). On the other hand, isotopic compositions of ions have not been detected, due to the difficulty in resolving the mass difference. The Martian Moons eXploration (MMX) mission, which is planned by the Japan Aerospace Exploration Agency to target the two Martian moons, with a scheduled launch in 2024 (Kuramoto et al. 2022), may measure the isotopic compositions of escaping ions. The mass spectrum analyzer, with unprecedented mass resolution, on board MMX will be able to measure the isotope ratios of escaping ion species, such as O^+ and C^+ (Yokota et al. 2021; Kuramoto et al. 2022; Ogohara et al. 2022). Such measurements can empirically constrain the fractionation factor by atmospheric escape and the history of the Martian atmosphere. On the other hand, it should be mentioned that if the photochemical loss of carbon as a neutral is dominant, the measurements of the isotope ratios would only constrain the fractionation of a small fraction of escaping carbon.

5. Conclusion

We have developed a 1D photochemical model to consider the carbon isotopic fractionation that is induced by the photolysis of CO_2 for the Martian atmosphere. According to our results, CO is depleted in ^{13}C compared with CO_2 at each altitude, due to the fractionation effect of photolysis. Below the homopause, the $\delta^{13}C$ in CO decreases as the altitude decreases: it takes about $-170‰$ near the surface under the standard eddy diffusion setting. Above the homopause, the $\delta^{13}C$ in both CO and CO_2 decreases as the altitude increases, due to the diffusive separation that results from the difference in molecular mass between isotopologues. Our results support the hypothesis that the fractionated atmospheric CO is responsible for the production of the ^{13}C-depleted organic carbon in Martian sediments, as detected by the Curiosity Rover, via the conversion of CO into organic materials and their deposition on the surface. The isotopic fractionation of CO by photolysis and the diffusive separation between the lower atmosphere and the escape region enhances the degree of fractionation through photochemical escape via CO photodissociation. The fractionation factor when considering these effects becomes lower than that evaluated by Hu et al. (2015): it changes from 0.60 to 0.52 under the standard eddy diffusion setting. The change in the fractionation factor may lead to a decrease in the amount lost by atmospheric escape, constrained by the evolution of the atmospheric carbon isotopic composition. The fractionated isotopic composition of the CO in the Martian atmosphere may be observed by the ExoMars TGO and ground-based telescopes, while the escaping ion species produced by the fractionated carbon-bearing species may be detected by MMX in the future.

We thank the anonymous reviewers whose comments greatly improved the manuscript. This work was supported by JSPS KAKENHI grant Nos. 22K03709, 22H05151, 22H00164, 19H00707, 18H05439, 18KK0093, 20H00192, 22KK0044, 20H04605, and 19K03943. Y.U. was also supported by JSPS KAKENHI grant Nos. 17H01165, 21H04513, 19H09160, and 22H01290. Y.N. was also supported by JSPS KAKENHI grant No. 22J14954 and the International Joint Graduate Program in Earth and Environmental Sciences, Tohoku University (GP-EES). N.Y. was also supported by JSPS KAKENHI grant No. 21J13710 and the International Joint Graduate Program in Earth and Environmental Sciences, Tohoku University (GP-EES). S.K. was also supported by JSPS KAKENHI grant No. 22K03709.

Appendix

In this appendix, chemical reactions used in the photochemical model are listed in Tables A1 and A2.

Table A1
Chemical Reactions

No.	Reaction			Reaction Rate Coefficient[a]	Column Rate[b] Standard Case	Small Eddy Case	Large Eddy Case
R1	$^{12}CO_2 + h\,\nu$	→	$^{12}CO + O$		1.3×10^{12}	1.2×10^{12}	1.4×10^{12}
R2		→	$^{12}CO + O(^1D)$		2.0×10^{11}	1.7×10^{11}	2.1×10^{11}
R3	$^{13}CO_2 + h\,\nu$	→	$^{13}CO + O$		1.2×10^{10}	1.1×10^{10}	1.2×10^{10}
R4		→	$^{13}CO + O(^1D)$		2.3×10^{9}	1.9×10^{9}	2.4×10^{9}
R5	$H_2O + h\,\nu$	→	$H + OH$		8.3×10^{9}	8.5×10^{9}	8.7×10^{9}
R6		→	$H_2 + O(^1D)$		5.7×10^{3}	5.7×10^{3}	5.7×10^{3}
R7	$O_3 + h\,\nu$	→	$O_2 + O$		7.1×10^{11}	5.9×10^{11}	1.3×10^{11}
R8		→	$O_2 + O(^1D)$		4.1×10^{12}	3.4×10^{12}	7.4×10^{11}
R9	$O_2 + h\,\nu$	→	$O + O$		1.3×10^{11}	1.3×10^{11}	2.8×10^{10}
R10		→	$O + O(^1D)$		1.6×10^{10}	5.7×10^{10}	2.5×10^{9}
R11	$H_2 + h\,\nu$	→	$H + H$		6.6×10^{4}	6.6×10^{4}	2.2×10^{5}
R12	$OH + h\,\nu$	→	$O + H$		9.0×10^{5}	6.0×10^{5}	1.0×10^{6}
R13		→	$O(^1D) + H$		4.4×10^{2}	8.8×10^{1}	4.8×10^{3}
R14	$HO_2 + h\,\nu$	→	$OH + O$		3.9×10^{10}	3.2×10^{10}	3.7×10^{10}
R15	$H_2O_2 + h\,\nu$	→	$OH + OH$		1.7×10^{11}	1.4×10^{11}	1.4×10^{11}
R16		→	$HO_2 + H$		1.7×10^{10}	1.4×10^{10}	1.4×10^{10}
R17		→	$H_2O + O(^1D)$		0	0	0
R18	$O + O + M$	→	$O_2 + M$	$5.4 \times 10^{-33}(300/T)^{3.25}$	2.3×10^{11}	2.7×10^{11}	8.2×10^{10}
R19	$O + O_2 + ^{12}CO_2$	→	$O_3 + ^{12}CO_2$	$1.5 \times 10^{-33}(300/T)^{2.4}$	4.9×10^{12}	4.1×10^{12}	9.4×10^{11}
R20	$O + O_3$	→	$O_2 + O_2$	$8.0 \times 10^{-12}\exp(-2060/T)$	3.7×10^{7}	4.3×10^{7}	7.0×10^{6}
R21	$O + ^{12}CO + M$	→	$^{12}CO_2 + M$	$2.2 \times 10^{-33}\exp(-1780/T)$	1.3×10^{8}	8.9×10^{7}	2.2×10^{8}
R22	$O + ^{13}CO + M$	→	$^{13}CO_2 + M$	$1.0074 \times 2.2 \times 10^{-33}\exp(-1780/T)$	1.2×10^{6}	8.3×10^{5}	2.1×10^{6}
R23	$O(^1D) + O_2$	→	$O + O_2$	$3.2 \times 10^{-11}\exp(70/T)$	2.4×10^{9}	2.8×10^{9}	1.0×10^{8}
R24	$O(^1D) + O_3$	→	$O_2 + O_2$	1.2×10^{-10}	8.4×10^{4}	1.5×10^{5}	2.2×10^{3}
R25	$O(^1D) + O_3$	→	$O + O + O_2$	1.2×10^{-10}	8.4×10^{4}	1.5×10^{5}	2.2×10^{3}
R26	$O(^1D) + H_2$	→	$H + OH$	1.2×10^{-10}	5.8×10^{7}	3.3×10^{7}	2.5×10^{8}
R27	$O(^1D) + ^{12}CO_2$	→	$O + ^{12}CO_2$	$7.5 \times 10^{-11}\exp(115/T)$	4.3×10^{12}	3.7×10^{12}	9.5×10^{11}
R28	$O(^1D) + H_2O$	→	$OH + OH$	$1.63 \times 10^{-10}\exp(60/T)$	8.5×10^{8}	5.3×10^{8}	1.6×10^{8}
R29	$H_2 + O$	→	$OH + H$	$6.34 \times 10^{-12}\exp(-4000/T)$	1.5×10^{6}	1.1×10^{6}	3.0×10^{7}
R30	$OH + H_2$	→	$H_2O + H$	$9.01 \times 10^{-13}\exp(-1526/T)$	1.3×10^{8}	1.2×10^{8}	1.5×10^{9}
R31	$H + H + ^{12}CO_2$	→	$H_2 + ^{12}CO_2$	$1.6 \times 10^{-32}(298/T)^{2.27}$	2.6×10^{5}	1.9×10^{5}	1.3×10^{7}
R32	$H + OH + ^{12}CO_2$	→	$H_2O + ^{12}CO_2$	$1.292 \times 10^{-30}(300/T)^{2}$	1.6×10^{5}	9.1×10^{4}	2.0×10^{6}
R33	$H + HO_2$	→	$OH + OH$	7.2×10^{-11}	7.0×10^{9}	5.7×10^{9}	6.6×10^{10}
R34	$H + HO_2$	→	$H_2O + O(^1D)$	1.6×10^{-12}	1.6×10^{8}	1.3×10^{8}	1.5×10^{9}
R35	$H + HO_2$	→	$H_2 + O_2$	3.45×10^{-12}	3.4×10^{8}	2.7×10^{8}	3.1×10^{9}
R36	$H + H_2O_2$	→	$HO_2 + H_2$	$2.8 \times 10^{-12}\exp(-1890/T)$	4.7×10^{5}	5.0×10^{5}	2.3×10^{6}
R37	$H + H_2O_2$	→	$H_2O + OH$	$1.7 \times 10^{-11}\exp(-1800/T)$	4.5×10^{6}	4.8×10^{6}	2.3×10^{7}
R38	$H + O_2 + M$	→	$HO_2 + M$	$k_0 = 8.8 \times 10^{-32}(300/T)^{1.3}$ $k_\infty = 7.5 \times 10^{-11}(300/T)^{-0.2}$	1.6×10^{12}	1.4×10^{12}	1.7×10^{12}
R39	$H + O_3$	→	$OH + O_2$	$1.4 \times 10^{-10}\exp(-470/T)$	6.8×10^{10}	8.0×10^{10}	7.5×10^{10}
R40	$O + OH$	→	$O_2 + H$	$1.8 \times 10^{-11}\exp(180/T)$	1.3×10^{11}	8.7×10^{10}	1.9×10^{11}

Notes.
[a] Two body: $cm^3\ s^{-1}$; three body: $cm^6\ s^{-1}$.
[b] $cm^{-2}\ s^{-1}$.

Table A2
Chemical Reactions

No.	Reaction			Reaction Rate Coefficient[a]	Column Rate[b]		
					Standard Case	Small Eddy Case	Large Eddy Case
R41	$O + HO_2$	$\rightarrow$	$OH + O_2$	$3.0 \times 10^{-11}\exp(200/T)$	1.2×10^{12}	1.1×10^{12}	1.3×10^{12}
R42	$O + H_2O_2$	$\rightarrow$	$OH + HO_2$	$1.4 \times 10^{-12}\exp(-2000/T)$	3.5×10^{7}	3.0×10^{7}	2.8×10^{7}
R43	$OH + OH$	$\rightarrow$	$H_2O + O$	1.8×10^{-12}	4.7×10^{5}	1.6×10^{5}	8.8×10^{5}
R44	$OH + OH + M$	$\rightarrow$	$H_2O_2 + M$	$k_0 = 8.97 \times 10^{-31}(300/T)$ $k_\infty = 2.6 \times 10^{-11}$	9.5×10^{3}	8.1×10^{3}	9.9×10^{3}
R45	$OH + O_3$	$\rightarrow$	$HO_2 + O_2$	$1.7 \times 10^{-12}\exp(-940/T)$	3.5×10^{6}	3.1×10^{6}	3.8×10^{5}
R46	$OH + HO_2$	$\rightarrow$	$H_2O + O_2$	$4.8 \times 10^{-11}\exp(250/T)$	6.0×10^{9}	5.6×10^{9}	4.3×10^{9}
R47	$OH + H_2O_2$	$\rightarrow$	$H_2O + HO_2$	1.8×10^{-12}	2.8×10^{9}	3.0×10^{9}	1.5×10^{9}
R48	$HO_2 + O_3$	$\rightarrow$	$OH + O_2 + O_2$	$1.0 \times 10^{-14}\exp(-490/T)$	4.2×10^{8}	2.5×10^{8}	7.0×10^{7}
R49	$HO_2 + HO_2$	$\rightarrow$	$H_2O_2 + O_2$	$3.0 \times 10^{-13}\exp(460/T)$	1.8×10^{11}	1.5×10^{11}	1.5×10^{11}
R50	$HO_2 + HO_2 + M$	$\rightarrow$	$H_2O_2 + O_2 + M$	$4.2 \times 10^{-33}\exp(920/T)$	6.4×10^{9}	5.6×10^{9}	4.9×10^{9}
R51	$^{12}CO + OH + M$	$\rightarrow$	$^{12}CO_2 + H + M$	$k_0 = 1.5 \times 10^{-13}(300/T)^{0.6}$ $k_\infty = 2.1 \times 10^{9}(300/T)^{-6.1}$	1.5×10^{12}	1.4×10^{12}	1.6×10^{12}
R52	$^{13}CO + OH + M$	$\rightarrow$	$^{13}CO_2 + H + M$	$k_0 = 0.9891 \times 1.5 \times 10^{-13}(300/T)^{0.6}$ $k_\infty = 0.9891 \times 2.1 \times 10^{9}(300/T)^{-6.1}$	1.4×10^{10}	1.3×10^{10}	1.5×10^{10}
R53	$^{12}CO + OH + M$	$\rightarrow$	$HO^{12}CO + M$	$k_0 = 5.9 \times 10^{-33}(300/T)^{1.4}$ $k_\infty = 1.1 \times 10^{-12}(300/T)^{-1.3}$	1.1×10^{10}	9.8×10^{9}	9.3×10^{9}
R54	$^{13}CO + OH + M$	$\rightarrow$	$HO^{13}CO + M$	$k_0 = 0.9891 \times 5.9 \times 10^{-33}(300/T)^{1.4}$ $k_\infty = 0.9891 \times 1.1 \times 10^{-12}(300/T)^{-1.3}$	9.9×10^{7}	8.9×10^{7}	8.7×10^{7}
R55	$HO^{12}CO + O_2$	$\rightarrow$	$HO_2 + ^{12}CO_2$	2.0×10^{-12}	1.1×10^{10}	9.8×10^{9}	9.3×10^{9}
R56	$HO^{13}CO + O_2$	$\rightarrow$	$HO_2 + ^{13}CO_2$	$0.9891 \times 2.0 \times 10^{-12}$	9.9×10^{7}	8.9×10^{7}	8.7×10^{7a}
R57	$^{12}CO_2^+ + H_2$	$\rightarrow$	$^{12}CO_2 + H + H$	8.7×10^{-10}	1.4×10^{8}	1.2×10^{8}	1.4×10^{9}

Notes.
[a] Two body: $cm^3\ s^{-1}$; three body: $cm^6\ s^{-1}$.
[b] $cm^{-2}\ s^{-1}$.

ORCID iDs

Shohei Aoki https://orcid.org/0000-0001-6727-125X
Naoki Terada https://orcid.org/0000-0001-5685-9736
Hiromu Nakagawa https://orcid.org/0000-0001-8166-0171
Shotaro Sakai https://orcid.org/0000-0001-9135-2076
Shungo Koyama https://orcid.org/0000-0002-5944-8948

References

Alday, J., Trokhimovskiy, A., Irwin, P. G., et al. 2021, NatAs, 5, 943
Aoki, S., Vandaele, A. C., Daerden, F., et al. 2019, JGRE, 124, 3482
Burkholder, J. B., Sander, S. P., Abbatt, J. P. D., et al. 2015, Chemical Kinetics and Photochemical Data for Use in Atmospheric Studies, Evaluation Number 18, Pasadena, CA: Jet Propulsion Laboratory, NASA
Chaffin, M. S., Deighan, J., Schneider, N. M., & Stewart, A. I. F. 2017, NatGe, 10, 174
Daerden, F., Neary, L., Viscardy, S., et al. 2019, Icar, 326, 197
Feilberg, K. L., Johnson, M. S., & Nielsen, C. J. 2005, PCCP, 7, 2318
Fox, J. L., & Bakalian, F. M. 2001, JGRA, 106, 28785
Fox, J. L., & Hac, A. B. 2009, Icar, 204, 527
Groller, H., Lichtenegger, H., Lammer, H., & Shematovich, V. I. 2014, P&SS, 98, 93
House, C. H., Wong, G. M., Webster, C. R., et al. 2022, PNAS, 119, e2115651119
Hu, R., Kass, D. M., Ehlmann, B. L., & Yung, Y. L. 2015, NatCo, 6, 10003
Huestis, D. L., & Berkowitz, J. 2011, PlSci, 25, 229
Hunten, D. M. 1982, P&SS, 30, 773
Jakosky, B. M. 1991, Icar, 94, 14
Jakosky, B. M., Pepin, R. O., Johnson, R. E., & Fox, J. L. 1994, Icar, 111, 271
Keller-Rudek, H., Moortgat, G. K., Sander, R., & Sorensen, R. J. E. S. S. D. 2013, ESSD, 5, 365
Korablev, O., Montmessin, F., Trokhimovskiy, A., et al. 2018, SSRv, 214, 1
Koyama, S., Terada, N., Nakagawa, H., Kuroda, T., & Sekine, Y. 2021, ApJ, 912, 135
Kuramoto, K., Kawakatsu, Y., Fujimoto, M., et al. 2022, EP&S, 74, 12
Kurokawa, H., Kurosawa, K., & Usui, T. 2018, Icar, 299, 443
Lammer, H., Scherf, M., Kurokawa, H., et al. 2020, SSRv, 216, 74
Lo, D. Y., Yelle, R. V., Lillis, R. J., & Deighan, J. I. 2021, Icar, 360, 114371
Nakamura, Y., Terada, K., Tao, C., et al. 2022a, JGRA, 127, e2022JA030312
Nakamura, Y., Terada, N., Koyama, S., et al. 2022b, arXiv:2301.02415
Ogohara, K., Nakagawa, H., Aoki, S., et al. 2022, EP&S, 74, 1
Owen, T., Biemann, K., Rushneck, D. R., et al. 1977, JGR, 82, 4635
Pepin, R. O. 1991, Icar, 92, 2
Pepin, R. O. 1994, Icar, 111, 289
Pickett, N. B., McFadden, J. P., Fowler, C. M., Hanley, K. G., & Benna, M. 2022, JGRA, 127, e2021JA029635
Pinto, J. P., Gladstone, G. R., & Yung, Y. L. 1980, Sci, 210, 183
Rayleigh, L. 1896, The London, Edinburgh, and Dublin Philosophical Magazine and Journal of Science, 42, 493
Schmidt, J. A., Johnson, M. S., & Schinke, R. 2013, PNAS, 110, 17691
Stueeken, E. E., Som, S. M., Claire, M., et al. 2020, SSRv, 216, 1
Ueno, Y., Schmidt, J. A., Johnson, M. S., et al. 2022, Anomalously 13C-depleted organic matter from CO in early Mars atmosphere, doi:10.21203/rs.3.rs-2312052/v1
Vandaele, A. C., Kruglanski, M., & De Maziere, M. 2006, in ESA SP-628, Modeling and Retrieval of Atmospheric Spectra Using ASIMUT, ed. H. Lacoste & L. Ouwehand (Paris: ESA), 71
Vandaele, A. C., Lopez-Moreno, J. J., Patel, M. R., et al. 2018, SSRv, 214, 80
Villanueva, G. L., Liuzzi, G., Aoki, S., et al. 2022, GeoRL, 49, e2022GL098161
Villanueva, G. L., Liuzzi, G., Crismani, M. M., et al. 2021, SciA, 7, eabc8843
Villanueva, G. L., Mumma, M. J., Novak, R. E., et al. 2013, Icar, 223, 11
Villanueva, G. L., Smith, M. D., Protopapa, S., Faggi, S., & Mandell, A. M. 2018, JQSRT, 217, 86
Webster, C. R., Mahaffy, P. R., Flesch, G. J., et al. 2013, Sci, 341, 260
Woods, T. N., Chamberlin, P. C., Harder, J. W., et al. 2009, GeoRL, 36, L01101
Yokota, S., Terada, N., Matsuoka, A., et al. 2021, EP&S, 73, 1
Yoshida, N., Nakagawa, H., Aoki, S., et al. 2022, GeoRL, 49, e2022GL098485